J. Fluid Mech. (1978), *vol.* 85, *part* 3, *pp.* 519–542
Printed in Great Britain

Supersonic flow of a vibrationally relaxing gas past a circular cone

By JAMES KAO† AND J. P. HODGSON
Department of the Mechanics of Fluids, University of Manchester, England

(Received 20 July 1977)

The steady supersonic flow of a vibrationally relaxing gas past a cone is studied using numerical methods. Near the tip of the cone the flow is obtained by means of a co-ordinate expansion and built on to this is a characteristic network used to obtain the remainder of the flow. Of particular interest is the development of the frozen shock at the tip into a relaxation-dominated wave at distances large compared with the width of the wave. The numerical results are presented in a concise similarity form which will permit accurate extrapolation to very weak waves in atmospheric air.

1. Introduction

Steady supersonic flows past pointed bodies of revolution have been extensively treated in the literature and for ideal gases difficulties associated with the singularity at the tip have long since been resolved. The flow past a cone at zero incidence was essentially solved by Taylor & Maccoll (1933) with numerical solutions by Kopal (1947).

Whereas the supersonic flow of an ideal gas past a symmetric wedge is separated by plane oblique shocks into regions of uniform flow, the equivalent axisymmetric flow past a cone consists of a locally plane shock followed by an isentropic compression which further deflects the streamlines parallel to the cone surface far downstream. According to the usual inviscid compressible flow assumptions both compressions take place at the tip for a cone surface streamline.

In the case of a vibrationally relaxing gas the initial change in properties on a cone surface streamline must be the same as for the ideal gas with specific heats equal to the frozen specific heats of the relaxing gas but thereafter the gas relaxes as it passes along the cone surface. The gas relaxes with vibrational energy increasing at the expense of ordered kinetic, rotational and translational energy. The rotational and translational energy modes are assumed to be in mutual equilibrium throughout the flow. One of the principal features of the flow is the attenuation of the frozen bow shock as its distance from the cone axis increases. Behind the decaying frozen shock a relaxation region develops, taking over an increasing fraction of the compression wave. As the distance tends towards infinity the structure of the wave approaches that of a plane oblique shock wave and behind it the flow is essentially in equilibrium. Unlike the wedge flows discussed by Hornby & Johannesen (1975), the flow downstream of the wave is non-uniform owing to axisymmetric effects even at large distances.

† Present address: Koninklijke/Shell Exploratie en Produktie Laboratorium, Volmerlaan 6, Rijswijk (Z.H.), Holland.

However, the wave at infinity contains all the properties discussed by them. As a one-dimensional wave it was described by Lighthill (1956) and it may be fully or partly dispersed. In this paper we are concerned with flows which lead to waves of both types.

The flow at infinity can be found by integrating the ideal-gas cone flow equations using the equilibrium properties of the gas. This gives only the strength and inclination of the wave but its detailed structure can then be determined by one-dimensional considerations as a separate exercise. Thus the flow changes from a frozen ideal-gas flow at the tip to an equilibrium ideal-gas flow at infinity, where the wave is of finite extent. To determine the flow we must find how this change takes place. Of particular interest is the development of the wave towards its ultimate 'one-dimensional' form and of the entropy layer caused by different streamlines having different early histories. As in the flow of an ideal gas, the streamlines approach the surface asymptotically. The entropy layer shrinks towards the body and might be expected to cause computational difficulties at large distances along the cone. Though we shall discuss flows past cones with semi-apex angles less than 15° the methods are directly applicable to cones having attached shocks and supersonic flow downstream.

A number of papers have presented approximate treatments of these flows but it is usually difficult to obtain precise numerical results which accurately account for the essentially nonlinear effects involved. Khodyko (1964) solved the linearized flow equations for the supersonic flow of a relaxing gas past a slender cone. Chou & Chu (1971) solved the nonlinear equations by a systematic perturbation method using characteristic parameters. In neither case was information given concerning the flow at large distances from the body. Very recently Clarke & Sinai (1977) used matched asymptotic expansions allowing certain regions of the flow to be calculated even in the far field. Their method consists of an extension of that of Blythe (1969) to axisymmetric flow and is for slender cones.

To obtain solutions which accurately describe the development of the wave towards its ultimate one-dimensional form at infinity, numerical methods must in general be used. We chose the method of characteristics, which has been extensively used to solve the hyperbolic equations of supersonic flow. The accuracy of this approach in non-equilibrium flows was demonstrated by Hornby & Johannesen (1975) and by Dain & Hodgson (1975). However, this method cannot be applied near the singularity at the tip of the cone and a suitable starting procedure must be developed. Sedney & Gerber (1963) initiated their calculations by assuming that the flow was frozen in a finite region surrounding the tip. This led to errors throughout the flow, but particularly just downstream of the frozen region. Later Sedney & Gerber (1967) calculated the first derivatives of the flow variables at the tip and these could have been used to determine more accurate starting conditions for the method of characteristics. The gradients were determined in a normalized stream-function co-ordinate system introduced by Chester (1956) and require transformation back to the physical plane.

Having available a large computer we found it simpler to use a direct approach to determine the flow in the neighbourhood of the tip. The thermodynamic variables were expressed as polar co-ordinate expansions about the tip and these were matched onto the curved frozen shock boundary. This approach was mentioned briefly by Sedney & Gerber (1967). Successive orders of the expansion were integrated numeri-

cally. Details of the tip expansion method are given in § 3, which may be bypassed to obtain the far-field results.

The flows investigated are particularly interesting since they shed some light on the behaviour of fully dispersed and weak partly dispersed waves subjected to axisymmetric propagation effects. It has been shown by Hodgson & Johannesen (1971) that such waves are present in the atmosphere as sonic bangs.

2. General requirements for the calculation procedure

The flow was considered in two distinct parts within which different methods were used to obtain numerical solutions. In the neighbourhood of the tip a co-ordinate expansion was used to solve the equations expressed in polar co-ordinates. At a finite distance from the tip the method of characteristics was used to continue calculation of the remainder of the flow. Both parts of the calculation were carried out in the physical plane. Non-dimensionalization of variables was based on free-stream conditions, denoted by a suffix ∞. A prime indicates a dimensional quantity and all unprimed variables are non-dimensional:

$$p' = p'_\infty p, \quad \rho' = \rho'_\infty \rho, \quad T' = T'_\infty T, \tag{1)–(3)}$$

$$(q', a', u', v') = (\mathscr{R}' T'_\infty)^{\frac{1}{2}} (q, a, u, v), \tag{4}$$

$$\sigma' = (\mathscr{R}' T'_\infty)\, \sigma, \quad \Phi' = \Phi'_\infty \Phi, \tag{5), (6)}$$

$$(c'_p, c'_{\mathrm{vib}}, s') = \mathscr{R}'(c_p, c_{\mathrm{vib}}, s) \tag{7}$$

and

$$(z', r', R', \ldots) = (\mathscr{R}' T'_\infty)^{\frac{1}{2}} / (\rho'_\infty \Phi'_\infty)\, (z, r, R, \ldots). \tag{8}$$

Here p, ρ and T are the pressure, density and translational temperature, q is the magnitude of the velocity vector, whose components are u and v, and a is the frozen speed of sound. σ is the vibrational energy, s is the entropy, c_p is the frozen specific heat at constant pressure, c_{vib} is the vibrational specific heat and $\mathscr{R}'$ is the gas constant. The relaxation frequency Φ is defined by the simple relaxation equation

$$D\sigma/Dt = \rho\Phi(\bar{\sigma} - \sigma), \tag{9}$$

where the bar denotes the local equilibrium value of σ, which is a function of T. Φ is also a function of T and the actual relationship depends on the particular gas. In the flows investigated the temperature changes are not very large. The general features of each flow will not be affected by putting

$$\Phi = 1, \quad d\bar{\sigma}/dT = c_{\mathrm{vib}} = \text{constant}. \tag{10), (11)}$$

The errors introduced by these simplifications will not exceed a few per cent. It is straightforward to include in the calculation the precise functional relationships $\Phi(T)$ and $\bar{\sigma}(T)$ for a particular gas with a consequent loss of generality. Taking the zero of both σ and $\bar{\sigma}$ to be their free-stream value allows us to write

$$\bar{\sigma} = c_{\mathrm{vib}}(T - 1). \tag{12}$$

Entropy is also measured from its free-stream value.

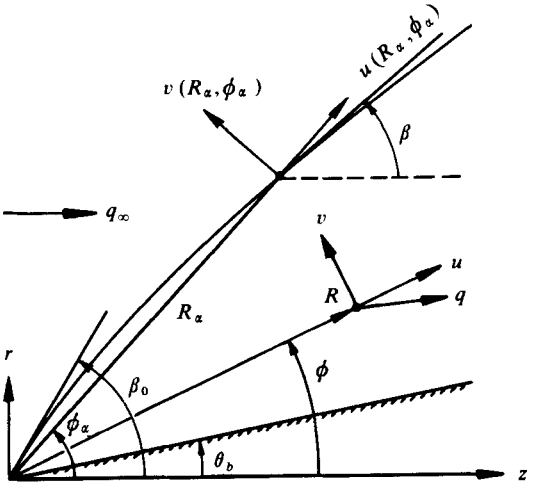

FIGURE 1. Co-ordinate systems and notation.

The frozen specific heats have also been assumed constant and all calculations presented here are for a gas with principal specific-heat ratio $\gamma = \frac{7}{5}$, which includes all diatomic and linear polyatomic gases. The equations of energy and state are used in both parts of the calculation and are valid throughout the flow:

$$c_p T + \sigma + \tfrac{1}{2}q^2 = c_p + \tfrac{1}{2}\gamma M_\infty^2, \tag{13}$$

$$p = \rho T, \tag{14}$$

where M_∞ is the Mach number based on the frozen speed of sound in the free stream. In general the frozen speed of sound is

$$a = (\gamma T)^{\frac{1}{2}}. \tag{15}$$

Viscosity and heat conduction have been neglected throughout. The restriction is no more severe than in ordinary ideal-gas compressible flow theory.

What follows is a detailed discussion of the methods used to determine a typical flow and the results are illustrated for the flow at $M_\infty = 2$ of a gas having $c_p = \frac{7}{2}$ and $c_{\text{vib}} = 1$ past a cone with a semi-apex angle of 10°.

3. The flow near the tip

The meridian plane of the spherical polar co-ordinate system with origin at the tip of the cone is shown in figure 1. The flow is axisymmetric, so that properties depend only on R and ϕ. The momentum equations in the R and ϕ directions are

$$Ru\frac{\partial u}{\partial R} + v\frac{\partial u}{\partial \phi} - v^2 + \frac{R}{\rho}\frac{\partial p}{\partial R} = 0 \tag{16}$$

and

$$Ru\frac{\partial v}{\partial R} + v\frac{\partial v}{\partial \phi} + uv + \frac{1}{\rho}\frac{\partial p}{\partial \phi} = 0. \tag{17}$$

The continuity equation is

$$R\frac{\partial u}{\partial R}+\frac{\partial v}{\partial \phi}+\frac{Ru}{\rho}\frac{\partial \rho}{\partial R}+\frac{v}{\rho}\frac{\partial \rho}{\partial \phi}+2u+v\cot\phi=0 \tag{18}$$

and the relaxation equation (9) becomes

$$Ru\frac{\partial \sigma}{\partial R}+v\frac{\partial \sigma}{\partial \phi}=\rho R\Gamma, \tag{19}$$

where

$$\Gamma=\bar{\sigma}-\sigma \tag{20}$$

is the local departure from equilibrium. These five equations together with (12)–(15) make up the required set. On eliminating p, $\bar{\sigma}$ and T using (12), (14) and (15) we find

$$v\frac{\partial \sigma}{\partial \phi}+R\left[u\frac{\partial \sigma}{\partial R}-\rho\Gamma\right]=0, \tag{21}$$

$$v\frac{\partial u}{\partial \phi}-v^2-R\left[\frac{1}{c_p}\frac{\partial \sigma}{\partial R}-\frac{u}{\gamma}\frac{\partial u}{\partial R}+\frac{v}{c_p}\frac{\partial v}{\partial R}-\frac{a^2}{\gamma\rho}\frac{\partial \rho}{\partial R}\right]=0, \tag{22}$$

$$\begin{aligned}(v^2-a^2)\frac{\partial v}{\partial \phi}+uv^2-a^2(2u+v\cot\phi)\\ +R\left[\frac{u}{c_p}\frac{\partial \sigma}{\partial R}+\left(\frac{u^2}{c_p}-a^2\right)\frac{\partial u}{\partial R}+\left(1+\frac{1}{c_p}\right)uv\frac{\partial v}{\partial R}-\frac{ua^2}{\gamma\rho}\frac{\partial \rho}{\partial R}-\frac{\rho\gamma\Gamma}{c_p}\right]=0,\end{aligned} \tag{23}$$

$$\begin{aligned}\frac{v(v^2-a^2)}{\rho}\frac{\partial \rho}{\partial \phi}+(u+v\cot\phi)v^2\\ -R\left[\frac{u}{c_p}\frac{\partial \sigma}{\partial R}+\left(\frac{u^2}{c_p}-v^2\right)\frac{\partial u}{\partial R}+\left(1+\frac{1}{c_p}\right)uv\frac{\partial v}{\partial R}-\left(v^2-\frac{a^2}{c_p}\right)\frac{u}{\rho}\frac{\partial \rho}{\partial R}-\frac{\gamma\rho\Gamma}{c_p}\right]=0,\end{aligned} \tag{24}$$

where

$$a^2=(\gamma-1)\left(c_p+\tfrac{1}{2}\gamma M_\infty^2-\sigma-\tfrac{1}{2}u^2-\tfrac{1}{2}v^2\right) \tag{25}$$

and

$$\Gamma=c_{\mathrm{vib}}(a^2/\gamma-1)-\sigma. \tag{26}$$

These are six equations for u, v, ρ, a, σ and Γ.

At the surface of the cone $v(R,\theta_b)=0$, where θ_b is the semi-apex angle of the cone. The shock location is given by $\phi_\alpha=\phi_\alpha(R_\alpha)$. At a point (R_α,ϕ_α) immediately behind the curved shock, which locally makes an angle β with the free stream, the flow must satisfy the oblique shock relations, i.e.

$$\sigma(R_\alpha,\phi_\alpha)=0, \tag{27}$$

$$u(R_\alpha,\phi_\alpha)\cos(\phi_\alpha-\beta)-v(R_\alpha,\phi_\alpha)\sin(\phi_\alpha-\beta)=\gamma^{\frac{1}{2}}M_\infty\cos\beta, \tag{28}$$

$$u(R_\alpha,\phi_\alpha)\sin(\phi_\alpha-\beta)+v(R_\alpha,\phi_\alpha)\cos(\phi_\alpha-\beta)=-\gamma^{\frac{1}{2}}\frac{(\gamma-1)M_\infty^2\sin^2\beta+2}{(\gamma+1)M_\infty\sin\beta} \tag{29}$$

and

$$\rho(R_\alpha,\phi_\alpha)=\frac{(\gamma+1)M_\infty^2\sin^2\beta}{(\gamma-1)M_\infty^2\sin^2\beta+2}. \tag{30}$$

In addition the following equation holds at the shock and may be used to find β:

$$\tan(\phi_\alpha-\beta)+R_\alpha d\phi_\alpha/dR_\alpha=0. \tag{31}$$

The equations were solved by expanding the dependent variables as a power series in R: for any variable ψ,

$$\psi(R,\phi) = \psi_0(\phi) + R\psi_1(\phi) + \tfrac{1}{2}R^2\psi_2(\phi) + \ldots, \tag{32}$$

where the function $\psi_i(\phi)$ can be recognized as the ith derivative with respect to R in the limit $R \to 0$. The shock location is given by the power series

$$\phi_\alpha(R_\alpha) = \phi_{\alpha 0} + R_\alpha \phi_{\alpha 1} + \tfrac{1}{2}R_\alpha^2 \phi_{\alpha 2} + \ldots, \tag{33}$$

where $\phi_{\alpha 0}, \phi_{\alpha 1}, \phi_{\alpha 2}, \ldots$ are constants. $\phi_{\alpha 0} = \beta_0$, the shock angle at the tip, and the local shock angle can also be expressed as a power series in R_α with constant coefficients:

$$\beta = \beta_0 + R_\alpha \beta_1 + \tfrac{1}{2}R_\alpha^2 \beta_2 + \ldots \ . \tag{34}$$

The equations governing the zeroth-order terms in the expansions defined by (33) were obtained by setting $R = 0$ in (21)–(24):

$$\frac{d\sigma_0}{d\phi} = 0, \quad \frac{du_0}{d\phi} = v_0, \tag{35), (36}$$

$$\frac{dv_0}{d\phi} = \frac{a_0^2(2u_0 + v_0 \cot\phi) - u_0 v_0^2}{v_0^2 - a_0^2}, \tag{37}$$

and

$$\frac{d\rho_0}{d\phi} = \frac{\rho_0 v_0 (u_0 + v_0 \cot\phi)}{a_0^2 - v_0^2}, \tag{38}$$

where

$$a_0^2 = (\gamma - 1)(c_p + \tfrac{1}{2}\gamma M_\infty^2 - \sigma_0 - \tfrac{1}{2}u_0^2 - \tfrac{1}{2}v_0^2). \tag{39}$$

The shock boundary conditions for these zeroth-order equations are given by setting $R_\alpha = 0$ in (27)–(31):

$$\sigma_0(\beta_0) = 0, \quad u_0(\beta_0) = \gamma^{\frac{1}{2}} M_\infty \cos\beta_0, \tag{40), (41}$$

$$v_0(\beta_0) = -\gamma^{\frac{1}{2}} \frac{(\gamma - 1) M_\infty^2 \sin^2\beta_0 + 2}{(\gamma + 1) M_\infty \sin\beta_\infty} \tag{42}$$

and

$$\rho_0(\beta_0) = \frac{(\gamma + 1) M_\infty^2 \sin^2\beta_0}{(\gamma - 1) M_\infty^2 \sin^2\beta_0 + 2}, \tag{43}$$

since $\phi_\alpha(0) = \beta_0$. The boundary condition on the body is simply $v_0(\theta_b) = 0$. As expected, the flow at the tip is frozen. Equations (36) and (37) are the well-known Taylor–Maccoll equations written in our notation. Numerical integration of these equations from the shock to the body was effected by use of the Runge–Kutta–Merson routine given in the *Nottingham Algorithms Group Library Manual* (1971). The angle $\beta_0 - \theta_b$ was divided into 50 equal segments and within each segment the library routine was applied with the size of the first step equal to 10^{-4} of the segment. The routine varies the step size automatically to keep the local truncation error below 10^{-12}. The integration was terminated when either $v_0 = 0$ or $\phi = \theta_b$. At the outset the value of β_0 corresponding to M_∞ and θ_b was unknown and to determine the appropriate value the integration was repeated with improved estimates of β_0 until $|v_0(\theta_b)| < 10^{-12}$.

Pictorial representation of the zeroth-order results is superfluous here but they were a necessary requirement for the solution of the higher-order equations, wherein zeroth-order variables appear as coefficients.

The equations governing first-order terms in the expansions defined by (32) were obtained by letting $R \to 0$ in the first partial derivatives with respect to R of (21)–(24). They are

$$\frac{d\sigma_1}{d\phi} + \frac{u_0 \sigma_1}{v_0} = \frac{\rho_0 \Gamma_0}{v_0}, \tag{44}$$

$$\frac{du_1}{d\phi} + \frac{u_0 u_1}{\gamma v_0} - \left(1 + \frac{1}{c_p}\right) v_1 - \frac{a_0^2 \rho_1}{\gamma \rho_0 v_0} = \frac{\sigma_1}{c_p v_0}, \tag{45}$$

$$\begin{aligned}(v_0^2 - a_0^2)\frac{dv_1}{d\phi} + \left[\frac{u_0^2}{c_p} + v_0^2 - 3a_0^2 + \frac{\gamma u_0 v_0^2}{c_p a_0^2}\left(\frac{dv_0}{d\phi} + u_0\right)\right] u_1 \\ + \left[(\gamma+1)\frac{v_0^3}{a_0^2}\left(\frac{dv_0}{d\phi} + u_0\right) - (2v_0^2 + a_0^2)\cot\phi - \frac{u_0 v_0}{\gamma}\right] v_1 - \frac{u_0 a_0^2}{\gamma \rho_0}\rho_1 \\ = \frac{\gamma \rho_0 \Gamma_0}{c_p} - \frac{1}{c_p}\left[u_0 + \frac{\gamma v_0^2}{a_0^2}\left(\frac{dv_0}{d\phi} + u_0\right)\right]\sigma_1 \end{aligned} \tag{46}$$

and

$$\begin{aligned}\frac{(v_0^2 - a_0^2) v_0}{\rho_0}\frac{d\rho_1}{d\phi} - \left[\frac{u_0^2}{c_p} - 2v_0^2 - \frac{\gamma u_0 v_0}{c_p \rho_0}\frac{d\rho_0}{d\phi}\right] u_1 \\ + \left[\frac{(\gamma+1) v_0^2}{\rho_0}\frac{d\rho_0}{d\phi} + 2v_0^2 \cot\phi - \frac{u_0 v_0}{c_p}\right] v_1 \\ + \left[v_0^2 (2u_0 + v_0 \cot\phi) - \frac{a_0^2 u_0}{c_p}\right]\frac{\rho_1}{\rho_0} \\ = -\frac{\gamma \phi_0 \Gamma_0}{c_p} + \frac{1}{c_p}\left(u_0 - \frac{\gamma v_0}{\rho_0}\frac{d\rho_0}{d\phi}\right)\sigma_1. \end{aligned} \tag{47}$$

The shock boundary conditions for these equations are given by differentiating (27)–(31) with respect to R_α and letting $R_\alpha \to 0$ along the shock:

$$\sigma_1(\beta_0) = 0, \tag{48}$$

$$u_1(\beta_0) = -\phi_{\alpha 1}[2\gamma^{\frac{1}{2}} M_\infty \sin\beta_0 + (du_0/d\phi)_{\phi=\beta_0} + v_0(\beta_0)], \tag{49}$$

$$v_1(\beta_0) = -\phi_{\alpha 1}\left[\frac{2\gamma^{\frac{1}{2}} \cos\beta_0 \{(\gamma-1) M_\infty^2 \sin^2\beta_0 - 2\}}{(\gamma+1) M_\infty \sin^2\beta_0} + \left(\frac{dv_0}{d\phi}\right)_{\phi=\beta_0} - u_0(\beta_0)\right], \tag{50}$$

$$\rho_1(\beta_0) = \phi_{\alpha 1}\left[\frac{8(\gamma+1) M_\infty^2 \sin\beta_0 \cos\beta_0}{[(\gamma-1) M_\infty^2 \sin^2\beta_0 + 2]^2} - \left(\frac{d\rho_0}{d\phi}\right)_{\phi=\beta_0}\right] \tag{51}$$

and

$$\beta_1 = 2\phi_{\alpha 1}. \tag{52}$$

In (44)–(52) all functions with suffix 0 are known from the zeroth-order solution. Initially $\phi_{\alpha 1}$ is unknown and to obtain its value we require that solution which satisfies the body boundary condition $v_1(\theta_b) = 0$.

Since boundary condition (48) is independent of $\phi_{\alpha 1}$, (44) can be solved separately and the solution is

$$\sigma_1(\phi) = \exp\left[-\int \frac{u_0}{v_0} d\phi\right]\left\{\int \frac{\rho_0 \Gamma_0}{v_0} \exp\left[\int \frac{u_0}{v_0} d\phi\right] d\phi + C\right\}, \tag{53}$$

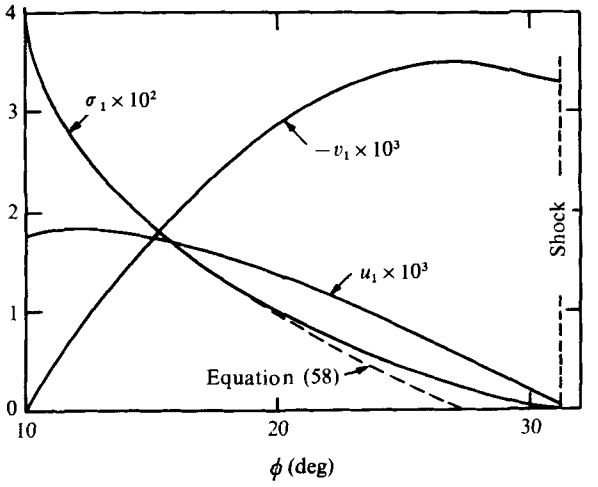

FIGURE 2. Gradients at the tip of the cone for $\gamma = \frac{7}{5}$, $c_{\text{vib}} = 1$, $M_\infty = 2$ and $\theta_b = 10°$. At $\phi = 10°$, $\sigma_1 = 4{\cdot}059 \times 10^{-2}$, $u_1 = 1{\cdot}755 \times 10^{-3}$.

where the constant of integration C is obtained using (48). Equations (45)–(47) are ordinary linear inhomogeneous differential equations in u_1, v_1 and ρ_1. One can, therefore, choose to write the solutions as

$$\psi_1(\phi) = \phi_{\alpha 1}\psi_1^{(h)}(\phi) + \psi_1^{(n)}(\phi), \tag{54}$$

where the $\psi_1^{(n)}$ are the solutions of (45)–(47) under boundary conditions (49)–(51) with $\phi_{\alpha 1} = 0$ and the $\psi_1^{(h)}$ are the solutions of the homogeneous equations obtained by equating the left-hand sides of (45)–(47) to zero under the same boundary conditions but this time with $\phi_{\alpha 1} = 1$.

The numerical integration of both homogeneous and inhomogenous equations was carried out in the same way as for the zeroth-order solution. When the body was reached the boundary condition allowed the determination of the scaling factor

$$\phi_{\alpha 1} = -v_1^{(n)}(\theta_b)/v_1^{(h)}(\theta_b). \tag{55}$$

The appearance of v_0 in the denominators of terms in the first-order equations indicates that the solutions may be singular on the body. To identify the nature of the singularity we proceed with analysis similar to that of Cabannes & Stael (1961).

In the neighbourhood of the body

$$u_0(\phi) = u_0(\theta_b) + O(\phi - \theta_b)^2 \tag{56}$$

and

$$v_0(\phi) = -2u_0(\theta_b)(\phi - \theta_b) + O(\phi - \theta_b)^2. \tag{57}$$

Substituting into (53) we obtain

$$\sigma_1(\phi) = \rho_0(\theta_b)\Gamma_0(\theta_b)/u_0(\theta_b) - c_1(\phi - \theta_b)^{\frac{1}{2}} + \ldots, \tag{58}$$

where c_1 is a constant. Clearly derivatives of σ_1 with respect to ϕ are singular on the body. Sedney & Gerber (1967) showed that the gradient functions in their co-ordinates possessed singularities of the same nature and for purposes of numerical integration they systematically reduced the step size near the body.

Equation (58) suggests that a Taylor series can be constructed for the gradient functions in the neighbourhood of the body using the transformation

$$\phi - \theta_b = \tfrac{1}{2}\delta^2. \tag{59}$$

Since the Runge–Kutta–Merson method is derived from the Taylor series, recasting (45)–(47) with δ as the independent variable should lead to a more accurate solution. First-order solutions in the ϕ and the δ co-ordinate agreed to four significant figures.

Results of the calculation of the first-order solution are illustrated in figure 2. The singular nature of the derivative of σ_1 at the cone surface is evident. The turning points in u_1 and v_1 were carefully investigated and are genuine properties of these functions.

Second-order equations were also obtained and solved using the same numerical approach with the appearance of no further singularities. We shall not discuss these equations here as only the first derivatives were used to start the characteristics network. However, some aspects of the second-order solution will be discussed briefly in comparison with the characteristics results.

4. The characteristics network

Outside the tip region the flow was calculated using the method of characteristics in cylindrical polar co-ordinates. The z axis was coincident with the axis of the cone with origin at the tip. The non-dimensionalized equations, in characteristic form, are

$$dr/dz = \tan(\theta + \mu), \tag{60}$$

$$\frac{dp}{\rho q^2 \tan\mu} + d\theta + \frac{(\gamma-1)\rho\Phi(\bar{\sigma}-\sigma)}{q^3 \sin\mu \sin(\theta+\mu)}\,dr = -\frac{\sin\mu\sin\theta}{r\sin(\theta+\mu)}\,dr \tag{61}$$

on the left-hand characteristics,

$$dr/dz = \tan(\theta - \mu), \tag{62}$$

$$\frac{dp}{\rho q^2 \tan\mu} - d\theta + \frac{(\gamma-1)\rho\Phi(\bar{\sigma}-\sigma)}{q^3 \sin\mu \sin(\theta-\mu)}\,dr = -\frac{\sin\mu\sin\theta}{r\sin(\theta-\mu)}\,dr \tag{63}$$

on the right-hand characteristics and

$$\frac{dr}{dz} = \tan\theta, \quad dp = -\rho q\,dq, \quad dr = \frac{\rho\Phi(\bar{\sigma}-\sigma)}{q\cos\theta}\,dz \tag{64)–(66}$$

on the streamlines. Here μ is the frozen Mach angle and θ the flow direction relative to the z axis. Equations (12)–(15) make up the required set. These equations are identical to those used by Hornby & Johannesen (1975) with the addition of the axisymmetric term on the right-hand sides of the compatibility equations. The boundary conditions are that $\theta = \theta_b$ on the body and that the oblique frozen shock relations must hold at the shock.

A network based on left-hand characteristics (CL) and streamlines (SL) and using interpolation along right-hand characteristics (CR) was chosen and is illustrated in figure 3. Within each network element the usual methods of iteration were employed for higher accuracy. The choice of network was based upon physical considerations. The two main effects in the flow are the propagation of disturbances from the body along CL's and the relaxation along SL's, whereas the CR's convey the much weaker

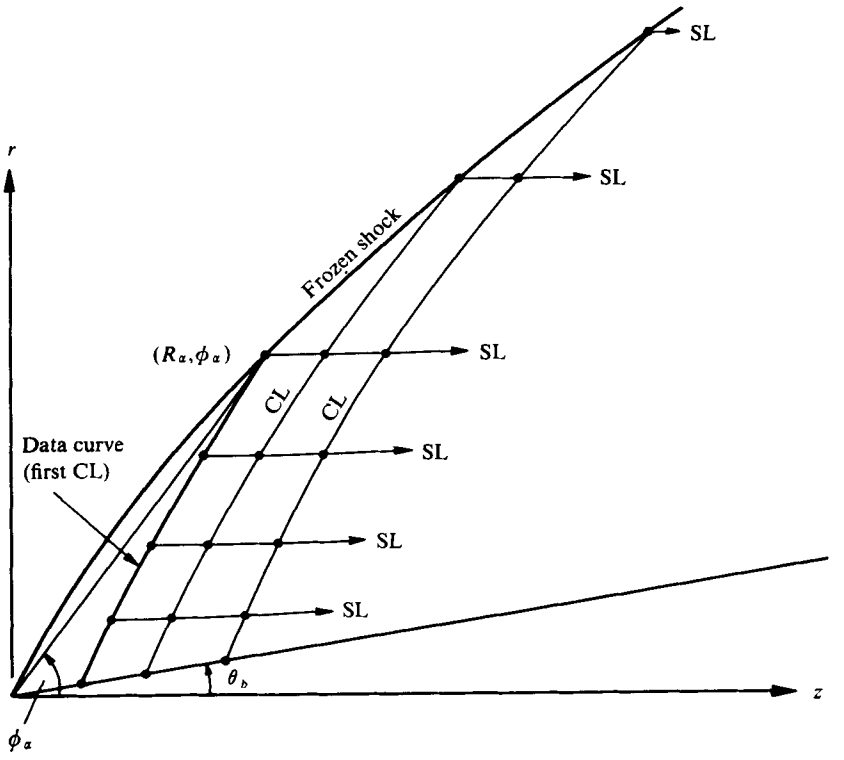

FIGURE 3. The characteristic network showing the starting procedure.

influence of the frozen shock on the flow nearer the body. With this network it was clear that the characteristics calculations should be started from a CL determined from the tip expansion solution described in § 3. The projection of the co-ordinate expansion solution onto a CL was incorporated as part of the numerical integration of the first-order terms, and all the flow variables were calculated at selected points along this first characteristic. These data points were chosen by consideration of the errors in the subsequent characteristics calculations and distributed such that equal changes in $\log r$ took place between adjacent points on the first CL. This distribution makes uniform the errors in the axisymmetric term of the compatibility relations. The reliability of the projection was tested by substituting the data into the compatibility equation. With the first CL intersecting the shock at $R_\alpha = 1$ and using steps of $\Delta(\log r) = 0{\cdot}1$, the compatibility equation was satisfied to within one part in 10^4. Changes in R_α and in $\Delta(\log r)$ led to systematic variations in the accuracy, which was also assessed using the second-order solution of the co-ordinate expansion. In the majority of flows calculated we used the numerical values of R_α and $\Delta(\log r)$ given above. This procedure created about 30 data points on the first characteristic. The streamlines through these points were used to build up the network in layers, each layer beginning at the body and ending at the frozen shock. Step sizes along the body were also chosen such that $\log r$ changed by the same amount between steps. This leads to larger step sizes downstream.

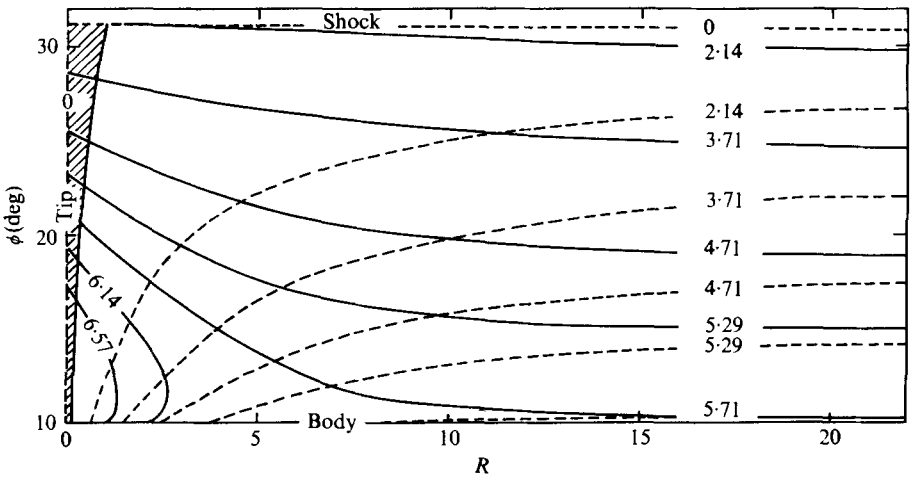

FIGURE 4. Contours of constant $10^2\bar{\sigma}$ (solid curves) and $10^2\sigma$ (dashed curves). The shaded area at small values of R denotes the region where the tip expansion was used. At the tip on the body $\bar{\sigma} = 0{\cdot}0761$. $\gamma = \frac{7}{5}$, $c_{\text{vib}} = 1$, $M_\infty = 2$ and $\theta_b = 10°$.

This particular way of increasing the step size along the body has essentially the same effect as the choice of a step size based on equal changes in a thermodynamic variable along the body. The latter method was used by both Hornby & Johannesen (1975) and Dain & Hodgson (1975). Both methods create small meshes where the flow gradients are large and both methods permit the calculation to proceed deep into the flow while making efficient use of computer storage capacity. However, the step size must not be allowed to increase indefinitely since this would lead to too much information being lost in the far field. For this reason the step size was increased no further after the frozen shock strength had decreased 90% of the way towards its ultimate value at infinity. In the case of a fully dispersed wave at infinity the frozen shock decays to zero strength. In the network this manifested itself by an overshoot to negative shock strength and, after interpolating to zero strength, the shock was replaced by a free-stream characteristic. The overshoot was in all cases less than 0·05% of the shock strength at the tip and replacement of the shock by a free-stream characteristic was no less accurate than any single network calculation.

The continuity equation was integrated along each CL and found to be satisfied to better than 1%. A further important check is possible since the exact flow at infinity is known *a priori*. The developing wave structure can at all stages be compared with that of the wave at infinity.

The streamlines converge towards the body as z increases. At large distances along the body the stream tubes become very narrow and the entropy gradients become correspondingly large. Though difficulties might be expected in calculating this part of the flow, none were found in spite of it being necessary, owing to stream-tube convergence, to interpolate along a CR crossing up to thirty streamlines. Difficulties would almost certainly have arisen if a different dependent variable, entropy for instance, had been used in preference to pressure, which is relatively unaffected by entropy in this part of the flow.

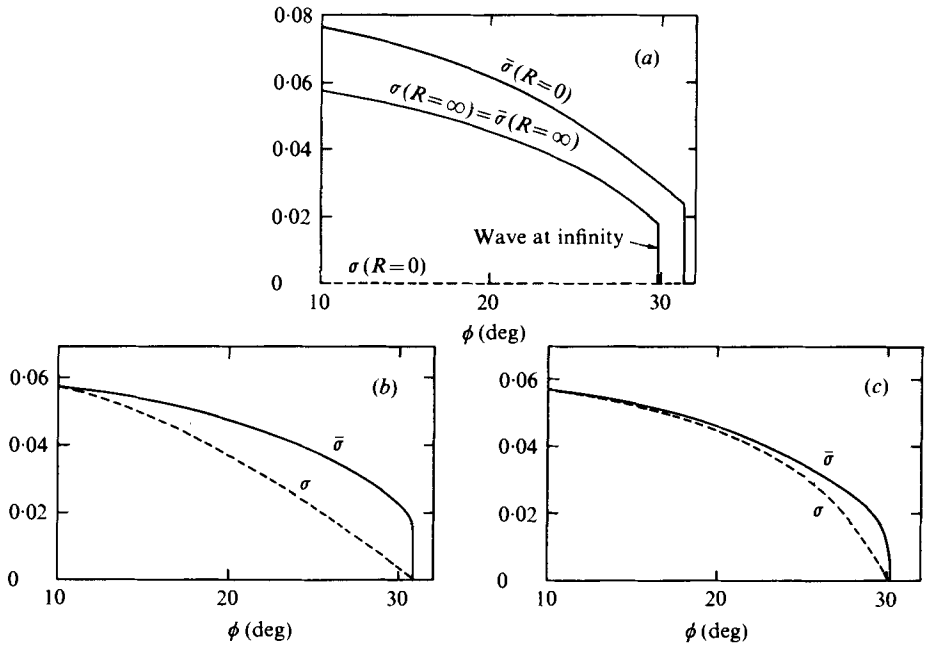

FIGURE 5. Sectional views of the $\bar{\sigma}$ and σ surfaces indicated in figure 4 at fixed values of R. (*a*) $R = 0$ and $R = \infty$, (*b*) $R = 10$ and (*c*) $R = 60$.

5. Detailed results for a particular flow

First, calculations were made for a gas having $c_{\text{vib}} = 1$ flowing past a cone with $\theta_b = 10°$ at $M_\infty = 2$. These conditions lead to a wave at infinity with a strength of about 85% of the maximum strength for a fully dispersed wave in a gas with $c_{\text{vib}} = 1$. For the same M_∞ and c_{vib} a cone angle of 10·4° would produce a maximum-strength fully dispersed wave at infinity. Left-hand characteristics were added to the network until $R \simeq 600$ along the frozen shock. By this stage the main features of the flow were included and what follows is a description of particularly interesting aspects of the results.

Conditions near the tip are indicated in figure 4, where contours of σ and $\bar{\sigma}$ are plotted in polar co-ordinates on rectangular axes. Such a plot stretches the tip singularity into a line. The σ and $\bar{\sigma}$ contours meet asymptotically as $R \to \infty$, where conditions depend only on ϕ and are described by the Taylor–Maccoll equations for the gas in equilibrium. Both $\bar{\sigma}$ and Γ, the local departure from equilibrium, have maxima at the tip on the body.

Sectional views of the contours in figure 4 are shown in figure 5. The extreme cases $R = 0$ and $R = \infty$ are shown in figure 5(*a*), where both flows are obtained from ideal-gas calculations using frozen-gas properties at $R = 0$ and equilibrium-gas properties at $R = \infty$. The non-equilibrium structure of the fully dispersed wave at infinity can be calculated from the equilibrium wave strength, but even so it would appear as a discontinuity in the figure. Figures 5(*b*) and (*c*) show sectional views at $R = 10$ and $R = 60$ respectively. The frozen shock decay and the decreasing value of ϕ at the wave front are typical of the whole flow in demonstrating the smooth transition of the frozen

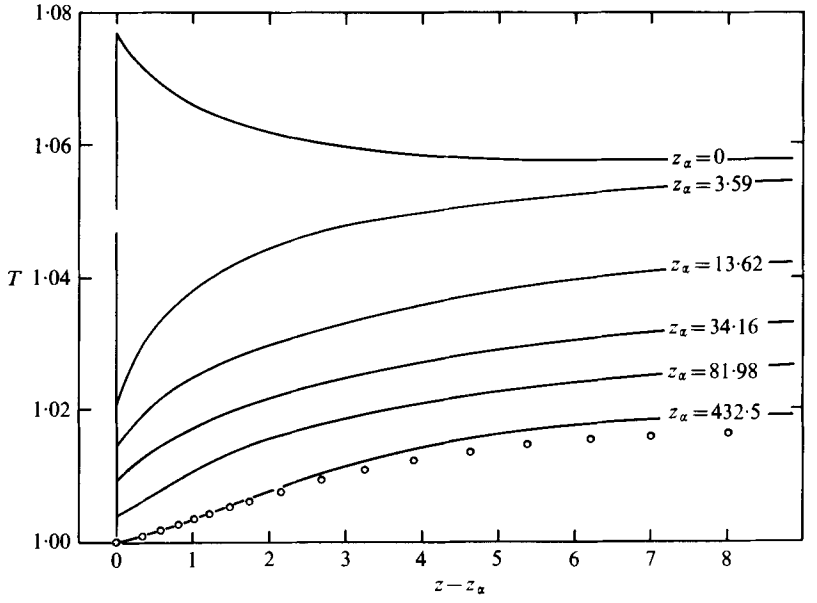

FIGURE 6. Temperature profiles of the developing wave along selected streamlines denoted by z_α, the co-ordinate at which the streamline intersects the frozen shock. The circles denote the profile of the wave at infinity.

flow at the tip into the equilibrium flow at infinity. Notice that equilibrium is reached very much more quickly near the body than near the wave, within which non-equilibrium effects persist to infinity.

The greatest departure from equilibrium occurs at the tip on the body. The rate of approach towards equilibrium is thus greater on the body streamline than on any other. The characteristics calculations indicated that along the body streamline equilibrium was approached exponentially with distance downstream from the tip. A more detailed investigation of the tip expansion, including second-order terms, showed that for this particular flow

$$\frac{\Gamma_2(\theta_b)}{\Gamma_0(\theta_b)}\Big/\left(\frac{\Gamma_1(\theta_b)}{\Gamma_0(\theta_b)}\right)^2 = 0{\cdot}9883, \tag{67}$$

where the suffixes on Γ denote the order of differentiation with respect to R in the limit $R \to 0$, defined according to (32). The proximity of the above numerical value to unity indicates that Γ exhibits almost exponential behaviour. Indeed, negligible differences occurred between the equation

$$\Gamma(R, \theta_b) = \Gamma_0(\theta_b) \exp\{R\Gamma_1(\theta_b)/\Gamma_0(\theta_b)\} \tag{68}$$

and the full characteristics solution over more than three orders of magnitude of variation in $\Gamma(R, \theta_b)$.

Of greater interest is the gradual evolution of the developing wave towards its final 'one-dimensional' wave structure. This is illustrated in figure 6, where the temperature along streamlines has been plotted against $z - z_\alpha$, where z_α is the z co-ordinate

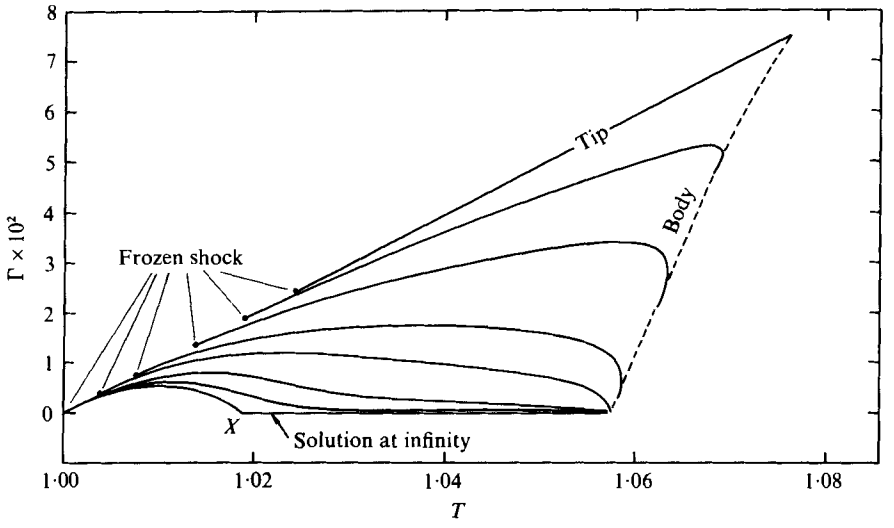

FIGURE 7. Local departure from equilibrium plotted against temperature along selected left-hand characteristics.

at which the streamline intersects the frozen shock. Also shown is the temperature profile of the one-dimensional wave at infinity. The actual location of the wave at infinity is not known *a priori* and in figure 6 the profile was matched by comparison with the front of the wave on the furthest calculated streamline. The influence of the non-uniform equilibrium core flow on the tail of the developing wave decreases as z_α increases. The influence is still in evidence for $z_\alpha = 432{\cdot}5$, but since the accumulated error in calculations to this stage is about 50% no real purpose would be served by computing much further. The trend is already clear. Figure 7 shows an alternative way of describing the thermodynamics of the entire flow. The local departure from equilibrium is plotted against temperature for selected left-hand characteristics. The gradual developments of the flow at the body, in the core and in the wave are evident even though they occur over quite different scales. Since the method of calculating the flow depends upon determining conditions on successive CL's, it is clear that the most inaccessible part of the flow is at the downstream side of the developing wave, near X in figure 7, where the flow at infinity is slowest to evolve. Note that the maximum value of Γ in the flow at infinity is an order of magnitude smaller than the maximum value at the tip.

There are two essentially different features of the development of the wave: the frozen shock and the relaxation region, which will be considered separately.

The decay of the frozen shock is represented in figure 8 by plotting

$$\log\{(\Gamma_\alpha - \Gamma_{\alpha\infty})/(\Gamma_{\alpha\infty} - \Gamma_{\alpha\infty})\}$$

against r. Here Γ_α is the departure from equilibrium behind the shock, $\Gamma_{\alpha 0}$ its value at the cone tip and $\Gamma_{\alpha\infty}$ its value at infinity. For fully dispersed waves (as in this particular example) $\Gamma_{\alpha\infty} = 0$.

For $r \leqslant 3$ the tip expansion adequately describes the decay (though it was *used* only for $r < 0{\cdot}5$), but thereafter the local logarithmic decay rate decreases, reaching

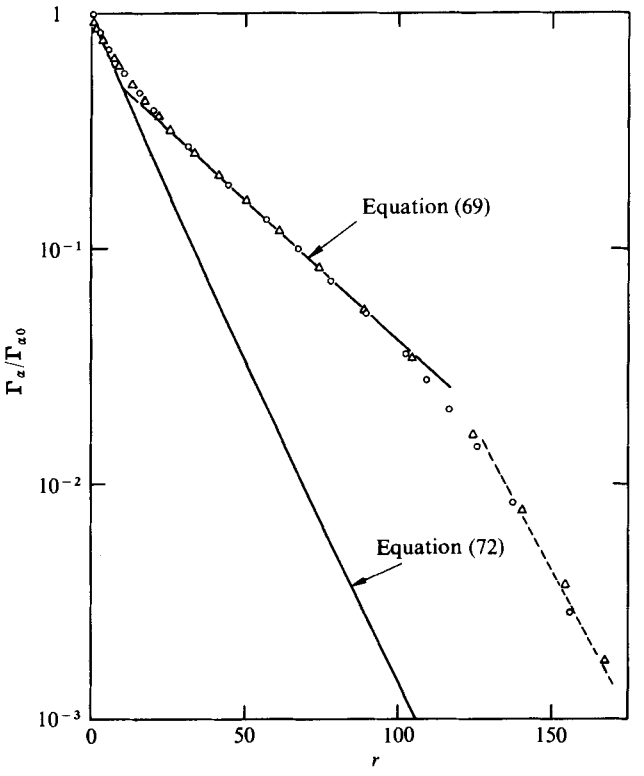

FIGURE 8. Frozen shock decay as a function of distance from the cone axis. The dashed line corresponds to the two-dimensional acoustic decay rate. Results are shown for two different step sizes: △, $\Delta(\log r) = 0{\cdot}05$; ○, $\Delta(\log r) = 0{\cdot}1$.

a nearly constant value in the range $20 \leqslant r \leqslant 100$. Following Hornby & Johannesen (1975), we shall approximate this part of the curve with the tangent at the point of greatest negative slope, described by the equation

$$(\Gamma_\alpha - \Gamma_{\alpha\infty})/(\Gamma_{\alpha 0} - \Gamma_{\alpha\infty}) = A \exp(-r/r_\alpha), \tag{69}$$

where A and r_α are empirical constants for each flow. Finally, the local logarithmic decay rate increases again. Only when $r > 100$ is there a significant difference between the results of calculations using two different step sizes determined by $\Delta(\log r) = 0{\cdot}1$ and $0{\cdot}05$. The difference is, of course, exaggerated by the logarithmic scale, since by this stage the strength of the shock is only a few per cent of its value at the tip. The smaller-step calculations are certainly more accurate but were too demanding on computer storage to be used for all subsequent flows. The ultimate logarithmic decay rate (in this case for $r > 130$) may be determined analytically using the following argument.

Since in steady axisymmetric flows of inviscid gases a stream surface may be replaced by a solid body of revolution, the same outer flow may be generated by a whole family of open-nosed bodies of revolution defined by stream surfaces nearer to the axis. Applying this well-known principle to the flow in the neighbourhood of the frozen shock when it becomes very weak leads to the conclusion that the ultimate

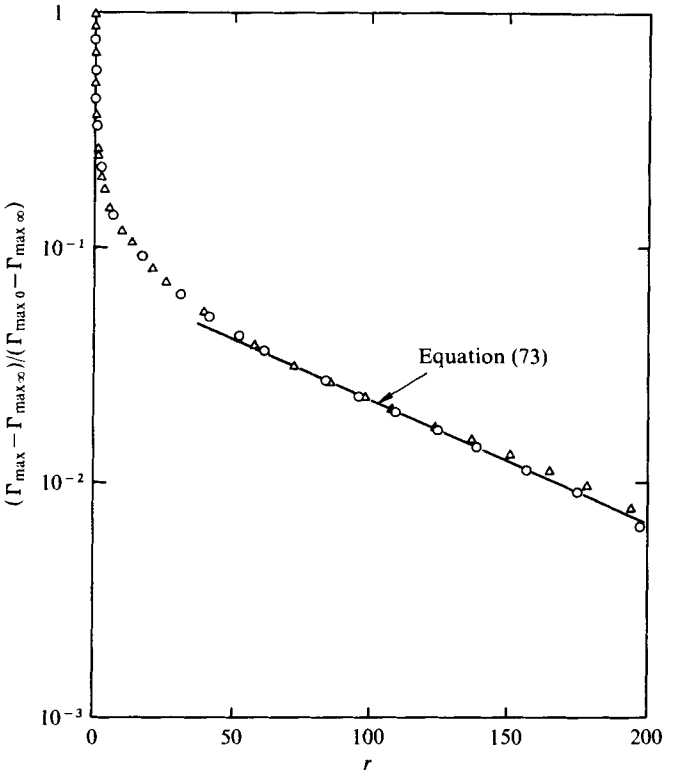

FIGURE 9. Development of the wave, represented by the maximum departure from equilibrium, towards its ultimate one-dimensional structure. △, $\Delta(\log r) = 0{\cdot}05$; ○, $\Delta(\log r) = 0{\cdot}1$.

decay of the frozen shock is determined by the flow past a thin *wedge*. Hornby & Johannesen (1975) give the decay law of such a shock:

$$\Gamma_\alpha = \Gamma_{\alpha 0} \exp(-y/y_{\alpha l}), \tag{70}$$

where

$$y_{\alpha l} = 2\gamma^{\frac{1}{2}}(M_\infty^2 - 1)^{\frac{1}{2}}/[(\gamma-1)^2 c_{v1b} M_\infty], \tag{71}$$

y is the co-ordinate distance measured normal to the free-stream direction and $y_{\alpha l}$ is the *two-dimensional* frozen acoustic decay distance. With y replaced by r, this frozen acoustic decay law is indicated by the dashed line in figure 8, where it is seen to describe the ultimate frozen shock decay. Only the slope of the dashed line and not the precise location is known *a priori*.

Also shown in figure 8 is the curve

$$\Gamma_\alpha = \tfrac{1}{2}\pi^{\frac{1}{2}}\Gamma_{\alpha 0}(y_{\alpha l}/r)^{\frac{1}{2}} \operatorname{erf}(r/y_{\alpha l})^{\frac{1}{2}} \exp(-r/y_{\alpha l}), \tag{72}$$

which is the slender-cone frozen shock decay law given by Chou & Chu (1971) and Clarke & Sinai (1977). As $r \to \infty$ the local logarithmic decay rates given by (70) and (72) coincide. The pre-exponential factors in (72) would modify the slope of the dashed line in figure 8 by only a few per cent. We shall find in the next section that our results are in agreement with (72) when $\theta_b \to 0$. Figure 8 demonstrates that the local logarithmic decay rate may be considerably slower than that given by (72) during the middle

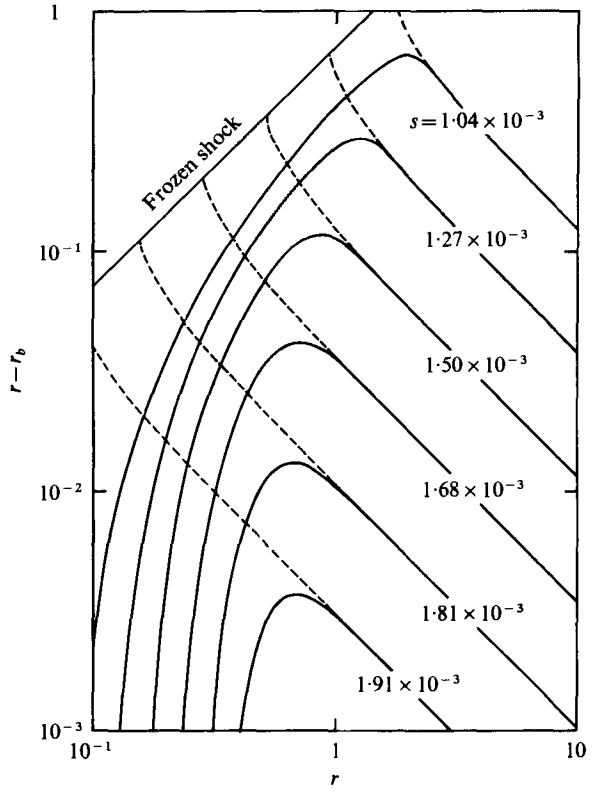

FIGURE 10. Entropy contours (solid curves) and streamlines (dashed curves) converging towards the cone surface. At the cone tip $s = 5{\cdot}73\times10^{-5}$.

part of its decay. The frozen acoustic decay law applies only when the shock strength has become about 1% of its tip value.

The development of the relaxation region into its ultimate form was given in figure 6. To describe the gross features of the wave we use a similar approach to that of Hornby & Johannesen (1975) and plot $\log\{(\Gamma_{\max}-\Gamma_{\max\infty})/(\Gamma_{\max 0}-\Gamma_{\max\infty})\}$ against r, as in figure 9. Here $\Gamma_{\max}$ is the maximum departure from equilibrium on a streamline, $\Gamma_{\max 0}$ its value on the body streamline and $\Gamma_{\max\infty}$ its value at infinity. The large gradient in this quantity at small distances occurs because the locus of $\Gamma_{\max}$ lies close to the cone surface near the tip. In this region changes in $\Gamma_{\max}$ are more closely related to the formation of the equilibrium core than to the developing wave. For $r \geqslant 10$, $\Gamma_{\max}$ depends essentially on the wave structure, while for $r \geqslant 50$, $\Gamma_{\max}$ is described by the empirical equation

$$(\Gamma_{\max}-\Gamma_{\max\infty})/(\Gamma_{\max 0}-\Gamma_{\max\infty}) = B\exp(-r/r_\beta), \tag{73}$$

where B and r_β are obtained by fitting the equation to the point of maximum negative slope in figure 9. For consistency in comparing different flows, calculations with a step size defined by $\Delta(\log r) = 0{\cdot}1$ were used. The results for $\Delta(\log r) = 0{\cdot}05$ lead to slightly different (better) values for the empirical constants but they are more than four times as expensive.

Entropy is produced in the flow by the frozen shock and by relaxation. Vincenti & Kruger (1965) show how the entropy increase due to relaxation may be obtained. Assuming the vibrational mode to be in internal equilibrium at temperature

$$T_{\mathrm{vib}} = 1 + \sigma/c_{\mathrm{vib}},$$

the entropy increase due to relaxation along a streamline is

$$ds = (1/T_{\mathrm{vib}} - 1/T)\,d\sigma. \tag{74}$$

This equation can then be integrated along any streamline starting in the free stream. Using assumptions outlined in § 2:

$$s = (\gamma - 1)^{-1} \log T - \log \rho + c_{\mathrm{vib}} \log (1 + \sigma/c_{\mathrm{vib}}). \tag{75}$$

It is interesting to plot contours of constant entropy in the logarithmically distorted co-ordinates shown in figure 10, where r_b is the co-ordinate of the cone surface and r is the contour co-ordinate at the same value of z. Also shown are the shock location and streamlines which coincide with the entropy contours far downstream. Clearly streamlines and entropy contours approach the cone surface as r^{-1} and maximum entropy occurs at the body. These results provide additional evidence that the calculations are behaving correctly even in regions of the flow where certain thermodynamic gradients become very large. In the corresponding wedge flow the entropy layer does not shrink towards the body.

6. Comparison of the wave development of several flows

The results described in §§ 3–5 were obtained for a selection of gases having $c_{\mathrm{vib}} = 1{\cdot}0$, $2{\cdot}0$ or $3{\cdot}0$ flowing with $M_\infty = 2{\cdot}0$ or $3{\cdot}0$ past cones with semi-apex angles θ_b in the range 5°–15°. Since the main objective was to determine the progress of the wave the two families of curves including those shown in figures 8 and 9 were investigated in greater detail. The flow parameters r_α, A, r_β and B were determined for each flow. These parameters describe the gross features of the developing wave in the far field. We recognize, of course, that in the case of a fully dispersed wave at infinity the frozen shock ultimately decays according to the frozen acoustic decay law. By this stage the strength of the frozen shock is only a few per cent of its value at the tip. Bearing in mind the outcome of the investigations of Hornby & Johannesen (1975), a similarity representation of the above four parameters was sought. They found that the most important aspect of any one wedge flow defined by M_∞, c_{vib} and the wedge angle θ_w was the strength of the wave at infinity in relation to the maximum strength of a fully dispersed wave for the same values of M_∞ and c_{vib}. The maximum-strength fully dispersed wave was created by a wedge angle θ_w^*. This led to plotting their quantities equivalent to r_α, A, r_β and B against θ_w/θ_w^*. Plots of A and B collapsed onto single curves and when the shock decay and wave development distances were normalized by the frozen acoustic decay distance $y_{\alpha l}$ [equation (71)] they too collapsed onto single curves.

For given values of M_∞ and c_{vib} the maximum strength and inclination of a fully dispersed wave at infinity can be found from the two-dimensional plane shock wave relations. The cone angle θ_b^* required to produce such a shock at infinity can then be found by integrating the equilibrium Taylor–Maccoll equations from the shock to the body.

The normalization factor for the shock decay and wave development distances is not so readily obtained. We have shown in the previous section that when the frozen shock becomes very weak it decays according to two-dimensional linearized theory and in a preliminary assessment of the results a plot of $r_\alpha/y_{\alpha l}$ *vs.* θ_b/θ_b^* led to a collapse of all points onto a single curve. However, as $\theta_b/\theta_b^* \to 0$ the values of $r_\alpha/y_{\alpha l}$ approached a value somewhat less than unity, indicating that $y_{\alpha l}$ was not the limiting value of r_α as $\theta_b \to 0$. In a further attempt to determine the limiting value of r_α we looked at the first-order tip expansion and calculated numerically

$$-r_{\alpha 0}^{-1} = \lim_{r\to 0}\left\{\frac{d}{dr}\log\left(\Gamma_\alpha/\Gamma_{\alpha 0}\right)\right\} = \sin\beta_0\frac{\Gamma_1(\beta_0)}{\Gamma_0(\beta_0)} \tag{76}$$

for successively smaller values of θ_b and constant c_{v1b} and M_∞. Suffixes 0 and 1 refer to the order of differentiation with respect to R at the tip of the cone. It was clear that

$$\lim_{\theta_b\to 0}\{r_{\alpha 0}/y_{\alpha l}\} = \tfrac{3}{4} = r_{\alpha l}/y_{\alpha l} \tag{77}$$

and the limit was independent of c_{v1b} and M_∞.

Subsequently it was found that differentiation of (72) yields the same result, i.e.

$$\lim_{r\to 0}\left\{\frac{d}{dr}\log\left(\Gamma_\alpha/\Gamma_{\alpha 0}\right)\right\} = -\frac{4}{3y_{\alpha l}} = -\frac{1}{r_{\alpha l}}. \tag{78}$$

Henceforth $r_{\alpha l}$ was used to normalize r_α and r_β. The resulting plots are shown in figures 11 (*a*)–(*d*).

The first three plots indicate the same type of similarity as was found by Hornby & Johannesen (1975) but figure 11 (*d*) proves the exception and this apparent discrepancy merits our first consideration.

In the case of wedge flows the locus of $\Gamma_{\max}$ coincides with the frozen shock near the tip. In cone flows the locus is behind the frozen shock and directed much closer to the body surface. Figure 4 shows that $\Gamma_{\max}$ has its greatest value at the tip *on the body*. Consequently variations in $\Gamma_{\max}$ are controlled by the relaxation region behind the shock within the non-uniform flow created by the axisymmetry. Figure 9 shows that a fourfold decrease in $\Gamma_{\max}$ occurs in the very small range $0 \leqslant r \leqslant 2$. Thus the intercept value B is determined by the near-field flow, for which there is no reason to expect the same type of similarity. Since the locus of $\Gamma_{\max}$ is swept back close to the body it is not surprising that the values of B decrease as M_∞ increases. In fact for the two values of M_∞ used it appears that B is inversely proportional to M_∞. The precise dependence of B on Mach number could be obtained by a more detailed examination of the locus of $\Gamma_{\max}$ in the expansion about the tip, but the main point is that B depends on the near-field flow, being more closely related to the development of the equilibrium core than to the development of the wave.

Figure 11 (*a*) shows that the far-field frozen shock decay distance may be up to seven times greater than the linearized decay distance $r_{\alpha l}$. In the limit of small cone angle the frozen shock decay approaches that given by (72), which is plotted in figure 8, where $c_{\mathrm{v1b}} = 1{\cdot}0$ and $M_\infty = 2{\cdot}0$. For partly dispersed waves at infinity the decay distance rapidly decreases as θ_b increases. The physical reason for the very sharp peak in the 'critical' case $\theta_b = \theta_b^*$ can be understood by considering the properties of the wave at infinity. The maximum-strength fully dispersed wave at infinity is parallel to the left-hand free-stream characteristics. The front of this wave

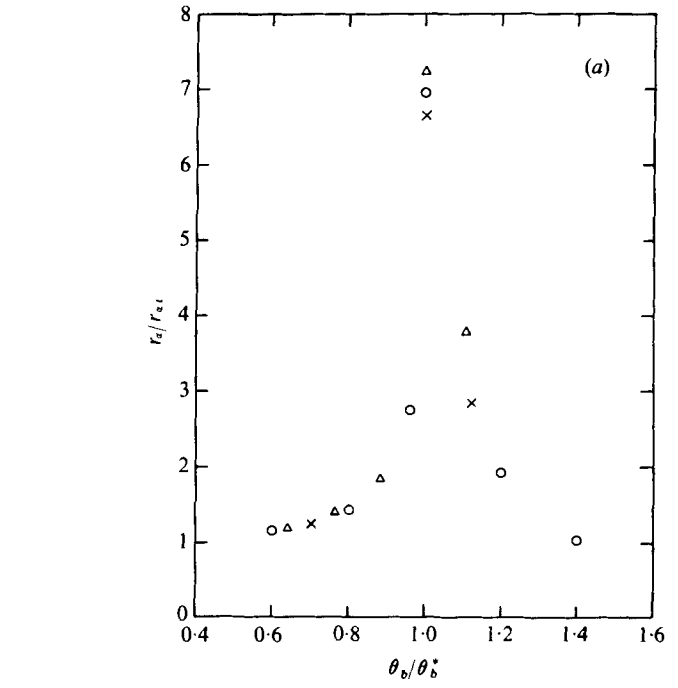

FIGURES 11(a, b). For legend see facing page.

is a zero-strength frozen shock across which there is a discontinuity in the gradient of thermodynamic quantities and which is approached asymptotically from behind by left-hand characteristics. Thus the information carried by the characteristics from the cone must travel a very great distance to reach the wave front. Those points for which $\theta_b < \theta_b^*$ lie very close to the fourth-power curve:

$$r_\alpha/r_{\alpha 1} - 1 = (\theta_b/\theta_b^*)^4. \tag{79}$$

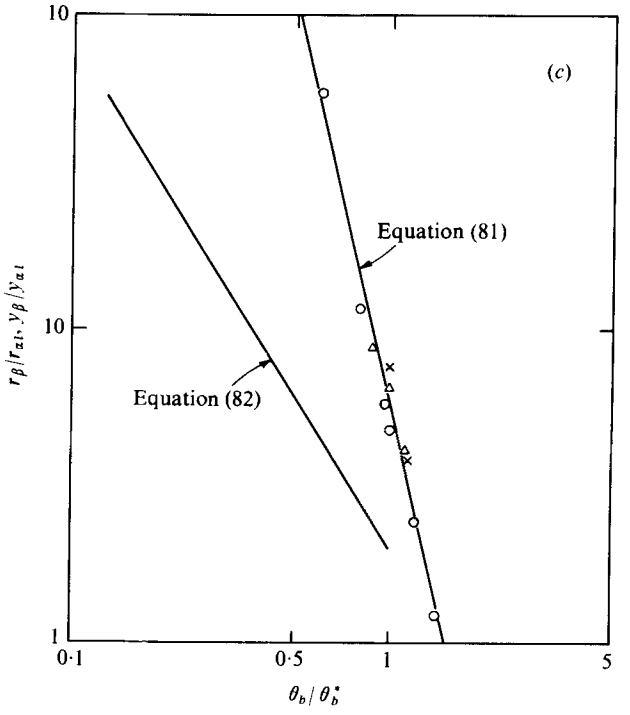

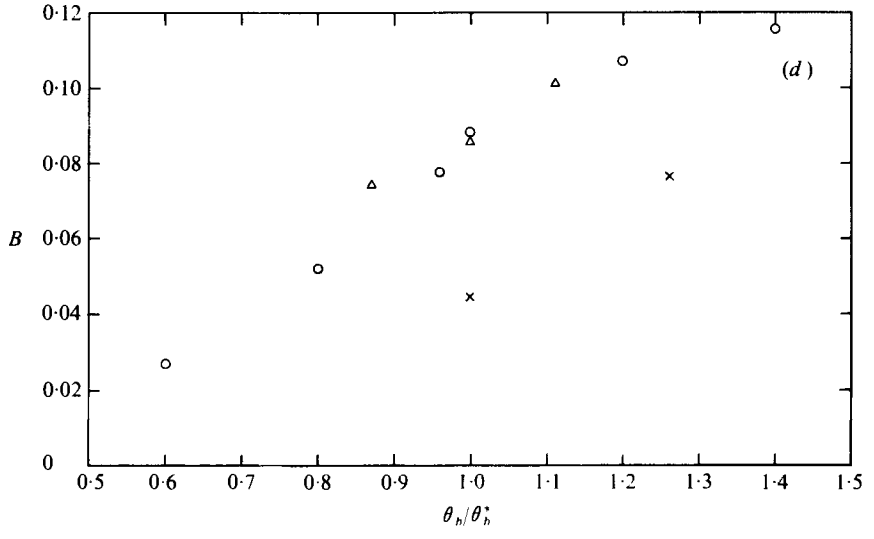

FIGURE 11. Normalized plots of (*a*) the far-field frozen shock decay distance, (*b*) the value of A defined by (69), (*c*) the far-field wave development distance and (*d*) the value of B defined by (73). ○, $M_\infty = 2$, $c_{\text{vib}} = 1$; △, $M_\infty = 2$, $c_{\text{vib}} = 3$; ×, $M_\infty = 3$, $c_{\text{vib}} = 1$. Also shown in (*c*) is the two-dimensional result, equation (82).

The results of Hornby & Johannesen (1975), for $\theta_w < \theta_w^*$, lie very close to the square law

$$y_\alpha/y_{\alpha l} - 1 = (\theta_w/\theta_w^*)^2, \tag{80}$$

where y_α is defined for plane flow in precisely the same way as r_α is defined for the cone flow.

For larger values of θ_b/θ_b^* the values of $r_\alpha/r_{\alpha l}$ decrease and approach the values of $r_\beta/r_{\alpha l}$ plotted in figure 11(*c*). This coincidence is to be expected since for strong partly dispersed waves $\Gamma_{\max}$ occurs immediately behind the frozen shock and so for large θ_b/θ_b^*, r_α and r_β measure the same effect. The values of r_β and B are in practice more inaccessible than those of r_α since the locus of $\Gamma_{\max}$ lies deep in the characteristic network behind the frozen shock. Consequently we do not have as many results. However, the trend of the points in figure 11(*c*) is clear and a least-squares fit to the available points is

$$r_\beta/r_{\alpha l} = 5{\cdot}7(\theta_b/\theta_b^*)^{-4{\cdot}3}. \tag{81}$$

Thus weaker fully dispersed waves require a much greater distance in which to develop their one-dimensional steady structure. For direct comparison the result for the wedge calculations is also shown:

$$y_\beta/y_{\alpha l} = 2{\cdot}0(\theta_w/\theta_w^*)^{-1{\cdot}6}, \tag{82}$$

where y_β is the plane flow parameter corresponding to r_β.

In figure 11(*b*) it is shown that the intercept value A has peculiar behaviour corresponding to that of r_α for θ_b in the neighbourhood of θ_b^*. For $\theta_b \to 0$, $A \to 1$ and $r_\alpha \to r_{\alpha l}$, and the frozen shock decay is described by (72). Since (72) describes also the shock decay in the very far field, where the frozen shock behaves as if it were very weak and two-dimensional, it appears that this equation describes the entire frozen shock decay in the limit $\theta_b \to 0$. This result agrees with the work of previous authors, for example Chou & Chu (1971) and Clarke & Sinai (1977).

Having shown that B is not directly a property of the wave development in the far field we conclude that the same type of similarity occurs for the cone as was shown to occur for the wedge. Figure 11 can be used to determine the gross aspects of wave development of cone flows of arbitrary Mach number in gases with arbitrary values of the vibrational specific heat.

7. Discussion and conclusion

It has been shown that the supersonic flow near the tip of a cone in a relaxing gas may be calculated by using a co-ordinate expansion procedure in polar co-ordinates and numerically integrating the equations of each order in the expansion. The tip flow was mapped onto a left-hand characteristic and the far field was calculated using the method of characteristics, which cannot be directly applied at the tip. Both parts of the calculation rely heavily on the use of a large computer to integrate equations which cannot at present be solved by analytical means.

The evolution of the frozen flow at the tip into an equilibrium flow, bounded by a 'one-dimensional' shock wave with relaxation, was traced. The main part of the development of the wave was then found to be described by empirical similarity laws. The similarity laws allow the determination of the gross features of the development of waves of arbitrary strength in gases with arbitrary vibrational specific heat. The

results, in particular (81), can be used to determine the development distances of waves in atmospheric air, where the dispersion may be due to the small contribution of the vibrational specific heats of oxygen and/or nitrogen. In this case the maximum-strength fully dispersed waves are in the noise intensity range currently causing most concern. In a completely different vibrational specific heat range the results could be used to calculate the structure of shock waves in the hot combustion products of a jet-engine exhaust. Though the cone is a wave source of infinite extent the methods described may be extended to deal with a finite body of revolution, for which the present paper may be regarded as a preliminary exercise.

Using the wedge results Hodgson & Johannesen (1976) estimated the development distances for waves in the atmosphere. The precise values are particularly sensitive to humidity variations but they depend also on ambient temperature and pressure and on wave strength. For wave strengths in the range 1–100 Pa development distances are likely to be between 0·1 and 100 km. Thus for a developing wave in the atmosphere it cannot be automatically assumed that conditions are uniform ahead of the wave. Figure 11 (*c*) shows that for the cone even greater development distances are required than for the wedge.

In the light of these results the application of asymptotic theories to describe long-distance sonic-bang or sound propagation in the atmosphere must be critically re-appraised. Vibrational relaxation and compressive steepening are certainly important features in all large amplitude disturbances but it is not obvious that the scale of the atmosphere permits the waves created to become fully developed.

Undoubtedly the weakness of loud noise waves and the smallness of the vibrational specific heats of atmospheric oxygen and nitrogen invite the use of approximate methods, such as those of Clarke & Sinai (1977). The characteristics method, with equations cast as in § 3, is not likely to be the best under such circumstances. However, the similarity laws obtained indicate that the main features of wave development depend on the ratio of the cone angle to the 'critical' cone angle which creates a maximum-strength fully dispersed wave at infinity. The critical cone angle depends on the free-stream gas properties. Though the calculations were made for c_{v1b} values considerably larger than for atmospheric oxygen or nitrogen the strengths of the waves investigated were also larger than, say, typical sonic-bang shocks, by a comparable factor. Thus extrapolation to the much weaker disturbances of loud noise in the atmosphere is valid.

Clarke & Sinai (1977) make no use of the exact wave solution at infinity, which for the cone is of finite strength. Their 'small-energy' approximation indicates the same type of similarity as has been found here, but in general their results also require numerical integration and considerably more work is required before we can make a direct comparison. In other cases their far-field flow is described by an axisymmetric form of Burgers' equation which is unlikely to describe accurately the wave at infinity unless it is very weak compared with the maximum-strength fully dispersed wave. The method is, however, applicable to bodies of finite size since Burgers' equation accurately describes the asymptotic flow at large distances. That the asymptotic solution is possible in the earth's atmosphere is again questionable.

The results of the characteristics calculations may be readily interpreted to obtain the gross features of shock wave development in the flow of any single-mode vibrationally relaxing gas past a cone.

We wish to thank Professor N. H. Johannesen and Dr I. M. Hall for many helpful discussions. The first author was in receipt of a Research Studentship from the S.R.C.

REFERENCES

BLYTHE, P. A. 1969 Non-linear wave propagation in a relaxing gas. *J. Fluid Mech.* **37**, 31.

CABANNES, H. & STAEL, C. 1961 Singularities of attached shock waves in steady axially symmetric flow. *J. Fluid Mech.* **10**, 289.

CHESTER, W. 1956 Supersonic flow past a bluff body with a detached shock. Part II. Axisymmetrical flow. *J. Fluid Mech.* **1**, 490.

CHOU, D. C. & CHU, B. T. 1971 On the decay of weak waves in axisymmetric non-equilibrium flow. *J. Fluid Mech.* **50**, 355.

CLARKE, J. F. & SINAI, Y. L. 1977 The wave system attached to a slender body in a supersonic relaxing gas stream. Basic results: the cone. *J. Fluid Mech.* **79**, 499.

DAIN, C. G. & HODGSON, J. P. 1975 The development of weak waves in the unsteady one-dimensional flow of a vibrationally relaxing gas ahead of an impulsively started piston. *J. Fluid Mech.* **69**, 129.

HODGSON, J. P. & JOHANNESEN, N. H. 1971 Real-gas effects in very weak shock waves in the atmosphere and the structure of sonic bangs. *J. Fluid Mech.* **50**, 17.

HODGSON, J. P. & JOHANNESEN, N. H. 1976 The effects of vibrational relaxation on the development of weak non-linear waves in air. *Proc. 6th Int. Symp. Non-Linear Acoust., Moscow State Univ.* pp. 30–40.

HORNBY, R. P. & JOHANNESEN, N. H. 1975 The development of weak waves in the steady flow of a gas with vibrational relaxation past a thin wedge. *J. Fluid Mech.* **69**, 109.

KHODYKO, Y. V. 1964 Flow of a relaxing gas around a thin cone of revolution. *N.A.S.A. Tech. Trans.* F-334.

KOPAL, Z. 1947 Tables of supersonic flow around cones. *M.I.T. Centre Anal. Rep.* no. 1.

LIGHTHILL, M. J. 1956 Viscosity in waves of finite amplitude. In *Surveys in Mechanics* (ed. Batchelor & Davies), pp. 250–351. Cambridge University Press.

SEDNEY, R. & GERBER, N. 1963 Non-equilibrium flow over a cone. *A.I.A.A. J.* **1**, 11.

SEDNEY, R. & GERBER, N. 1967 Shock curvature and gradients at the tip of pointed axisymmetric bodies in non-equilibrium flow. *J. Fluid Mech.* **29**, 765.

TAYLOR, G. I. & MACCOLL, J. W. 1933 The pressure on a cone moving at high speeds. *Proc. Roy. Soc.* A **139**, 838.

VINCENTI, W. G. & KRUGER, C. H. 1965 *Physical Gas Dynamics*, pp. 206 *et seq.* Wiley.